Precambrian Research 345 (2020) 105757

Contents lists available at ScienceDirect

Precambrian Research

journal homepage: www.elsevier.com/locate/precamres

Petrography and sulfur isotopic compositions of SEDEX ores in the early Cambrian Nanhua Basin, South China

Tao Han[a,b,*], HaiFeng Fan[a,b], HanJie Wen[a,b], Bing Mo[a,b], James B. Murowchick[c], ZhiTong Lu[a,b], Thomas J. Algeo[d,e,f]

[a] State Key Laboratory of Ore Deposit Geochemistry, Institute of Geochemistry, Chinese Academy of Sciences, Guiyang 550081, China
[b] University of Chinese Academy of Sciences, Beijing 100049, China
[c] Department of Geosciences, University of Missouri-Kansas City, Kansas City, MO 64110, USA
[d] Department of Geology, University of Cincinnati, Cincinnati, OH 45221-0013, USA
[e] State Key Laboratory of Geological Processes and Mineral Resources, China University of Geosciences, Wuhan 430074, China
[f] State Key Laboratory of Biogeology and Environmental Geology, China University of Geosciences, Wuhan 430074, China

ARTICLE INFO

Keywords:
Sulfide mineralization
Sulfur isotope
Microbial sulfate reduction
Bacterial sulfate reduction
Exhalative
Hydrothermal

ABSTRACT

Widespread Ni-Mo sulfide mineralization in South China during the early Cambrian may have affected the seawater chemistry and biodiversity of this region, but its underlying causes are not well-understood. To better understand the formation of sulfide ores in early Cambrian marine systems, this study evaluated the paragenesis and sulfur isotopic composition ($\delta^{34}S$) of sediment-hosted Ni-Mo sulfide ores in the lower Cambrian Niutitang Formation of the Nanhua Basin of South China. Petrographic analysis revealed three types of sulfide aggregates: (1) ubiquitous framboidal and euhedral pyrite (Py-1), (2) a MoSC phase (i.e., Mo mineralization) that was cogenetic with larger pyrite cubes or nodules (Py-2), and (3) intergrown millerite (NiS), sphalerite (ZnS) and veined pyrite (Py-3) (i.e., Ni-Zn mineralization) characterized by laminated and veined textures. Alternating precipitation of Mo and Ni-Zn sulfides was caused by intermittent emission of Mo-Fe or Ni-Zn-rich hydrothermal fluids into euxinic mid-depth waters of the Nanhua Basin, representing a sedimentary exhalative (SEDEX) process. The different sedimentary ore textures are each associated with a characteristic $\delta^{34}S$ distribution. At all study sites, the syngenetic Py-1 phase yields $\delta^{34}S$ of −15.7 to + 1.9‰, consistent with a seawater sulfate source that was variably fractionated through microbial sulfate reduction (MSR). In the Nayong and Zunyi areas, $\delta^{34}S$ values of −11.8 to +4.4‰ are associated with the MoSC phase, and −20.6 to −6.8‰ with the Py-2 phase. In the Zhangjiajie area, Py-2 yields similar values (−25.1 to −10.8‰) but MoSC higher and less variable values (+8.6 to +18.7‰). These phases are thought to contain a mixture of sulfur sourced from seawater sulfate (via MSR) and hydrothermal fluids in varying proportions. A mode of Ni-Zn sulfides $\delta^{34}S$ values between −9.1 and +8.0‰ is likely to represent the isotopic composition of hydrothermal sulfur inputs to the Ni-Zn mineralization. As a consequence, both hydrothermal emissions and biogenic production of H_2S had a significant influence on seawater chemistry, with consequences for contemporaneous evolution of early marine animal life (e.g., the small shelly fauna and Chengjiang Biota) in the early Cambrian Nanhua Basin.

1. Introduction

The nature of marine sedimentary deposits through Earth history has been closely related to the evolution of atmosphere-ocean system (Lyons et al., 2006; Pufahl and Hiatt, 2012). Some sedimentary ores such as banded iron formations (BIF), phosphorite beds and sedimentary exhalative (SEDEX) deposits were partially or completely derived from seawater, affecting the oceanic environment (Lyons et al., 2006; Pufahl and Hiatt, 2012; Leach et al., 2010). Large-scale submarine metallogenic events can affect the oceanic sulfur cycle, even though it is dominated by riverine source fluxes related to oxidative weathering of sulfide to sulfate on land and by sink fluxes related to evaporites and sedimentary pyrite (Rees, 1970; Bottrell and Newton, 2006; Halevy et al., 2012). All of these processes contribute to long-term secular changes in the oceanic sulfate reservoir and the sulfur isotope composition ($\delta^{34}S$) of seawater sulfate (Brennan et al., 2004; Fike and Grotzinger, 2008; Algeo et al., 2015). SEDEX deposits (e.g., Pb-Zn or pyrite) can exhibit a large range of sulfur isotope fractionations relative

* Corresponding author at: State Key Laboratory of Ore Deposit Geochemistry, Institute of Geochemistry, Chinese Academy of Sciences, Guiyang 550081, China.
E-mail address: hantao@mail.gyig.ac.cn (T. Han).

https://doi.org/10.1016/j.precamres.2020.105757
Received 12 December 2019; Received in revised form 8 March 2020; Accepted 20 April 2020
Available online 22 April 2020
0301-9268/

to ambient seawater, reflecting strong activity of sulfate-reducing microbes (SRM) under anoxic conditions (Goodfellow, 1987; Leach et al., 2005; Gadd et al., 2016, 2017; Qiu et al., 2018). Hydrothermal activity can also produce sediment-hosted massive barite deposits formed through mixing of barium-rich fluids and sulfate-rich seawater (Clark et al., 2004). The strong ^{34}S-enrichment of such deposits is thought to result from Rayleigh distillation of aqueous sulfate in restricted marine settings (Clark et al., 2004; Johnson et al., 2009). Hence, sulfide and sulfate mineralization processes can potentially affect seawater chemistry at a local or even a global scale.

The early Cambrian was a critical transitional interval in terms of both the Earth's surface oxygenation history and the diversification of early skeletonized metazoans (Sperling et al., 2013; Lyons et al., 2014). In South China, previous studies have shown a progressive shift from anoxic (ferruginous or euxinic) to oxic conditions in the mid-depth oceanic water mass, which may have triggered proliferation of the Chengjiang Biota (Wang et al., 2012; Wen et al., 2015; Jin et al., 2016; Zhao et al., 2018; Zhao et al., 2019). Although numerous types of geochemical data (e.g., redox-sensitive elements, iron speciation, and carbon, sulfur, nitrogen and molybdenum isotopes) have been collected for lower Cambrian successions in South China (Feng et al., 2014; Goldberg et al., 2007; Jin et al., 2016; Wang et al., 2012; Wen et al., 2015; Xu et al., 2020), the reason for formation of widespread Ni-Mo sulfide ores in these strata remains controversial. Existing models have proposed seawater sources (Lehmann et al., 2007; Xu et al., 2013), hydrothermal sources (Coveney and Chen, 1991; Lott et al., 1999; Jiang et al., 2007a; Han et al., 2017), biological enrichments (Cao et al., 2013), and multiple sources, e.g., mixing of seawater, terrigenous and hydrothermal inputs (Pašava et al., 2008) based on mineralogical and geochemical data such as trace elements, PGE and REE patterns, and Mo and Os isotopes. However, the poorly-defined paragenesis of these sulfide ores renders the existing geochemical data regarding metal and sulfur sources inadequate to evaluate these models. Furthermore, these sediment-hosted Ni-Mo sulfide ores, slightly predate the Chengjiang Biota (Jin et al., 2016) and thus have the potential to yield insights into oceanic environmental changes during the emergence of early animal life.

Here, we undertake an integrated study of the paragenesis and sulfur isotopic composition of sediment-hosted Ni-Mo sulfide ores in the lower Cambrian Niutitang Formation at open pits in Guizhou and Hunan provinces with the goal of investigating the formation of widespread lower Cambrian sedimentary sulfide deposits in the Nanhua Basin of South China. With the addition of published results from black shales of the lower Cambrian strata, this study provides a better understanding of the links between the seawater chemistry, sulfide mineralization, and co-evolution of marine life and environments in South China during the early Cambrian.

2. Geological background

The South China Craton was assembled during the early Neoproterozoic from the Yangtze and Cathaysia blocks, whose boundary is within the deep-water Nanhua Basin, a failed intracratonic rift basin that developed during the late Neoproterozoic (Feng et al., 2002; Li et al., 2008; Fig. 1A–B). Well-preserved lower Cambrian strata are underlain by dolostone of the upper Ediacaran Dengying Formation in shelf areas and by chert of the Liuchapo/Laobao formations in slope and basinal areas (Chen et al., 2009). On the Yangtze Platform, the Ediacaran-Cambrian boundary is identified by a negative shift in the carbon isotopic composition of shallow-water carbonates (i.e., the BACE event, Zhu et al., 2019). In slope and basinal facies, tuffaceous beds within the Liuchapo Formation have yielded ages of ~545–542 Ma, placing them close to the Ediacaran-Cambrian boundary (Chen et al., 2015). Early Cambrian seas of the South China Craton were characterized by a redox-stratified structure with an oxic surface layer, a ferruginous deep layer, and (locally) a euxinic mid-depth wedge (Feng et al., 2014; Wen et al., 2015; Jin et al., 2016).

Sediment-hosted Ni-Mo sulfide ores are mainly found in black shales of the lowermost Cambrian Niutitang Formation, which are widely distributed along the southern margin of the Yangtze Platform (Fig. 1B). These deposits contain up to 7% Ni, 8% Mo, 12% Zn and 12% total organic carbon (TOC) by weight, but they are often only a few centimeters thick (Han et al., 2015a,b). These widespread Ni-Mo sulfide ores formed at 521 ± 5 Ma based on Re-Os dating (Xu et al., 2011). They are present at a specific stratigraphic level within the Niutitang Formation, which consists (in ascending order) of a basal phosphorite layer, a volcanic tuff, a chert layer, a lower black shale containing phosphate nodules, large carbonate concretions, and a Ni-Mo sulfide layer, and, finally, an upper black shale, as seen in the Nayong and Zunyi areas of Guizhou Province and the Zhangjiajie area of Hunan Province (Li, 1997; Han et al., 2017; Fig. 1C). The sulfide ores were deposited in outer shelf settings under anoxic ferruginous and intermittently euxinic conditions, as inferred from analysis of Fe speciation and redox-sensitive trace elements in the enclosing black shales (Jin et al., 2016; Han et al., 2018).

3. Samples and methods

3.1. Samples

Sediment-hosted Ni-Mo sulfide ore samples from the lowest Cambrian Niutitang Formation were collected for this study (Fig. 1B-C). In Guizhou Province, three samples were collected from open pits of the Nayong area (26°44′13″ N, 115°36′12″ E) and nine samples from open pits of the Zunyi area (27°41′22″ N, 106°40′37″ E). In Hunan Province, three samples were collected from open pits in the Zhangjiajie area (29°11′7″ N, 110°54′47″ E). The thickness of the sulfide ores is similar in all three study areas, generally ranging from 2 to 5 cm (Supplementary Materials).

3.2. Methods

All samples were cut and prepared as polished sections. Petrographic observation was performed using a FEI Scios DualBeam field emission scanning electron microscope (FESEM) system equipped with EDAX Energy Dispersive Spectroscopy (EDS) at the Center for Lunar and Planetary Sciences, Institute of Geochemistry, Chinese Academy of Sciences (IGCAS) in Guiyang, Guizhou Province. The EDS point analysis and backscatter electron (BSE) mode analysis were carried out at 20 kV for mineral identification and mapping.

Samples for sulfur isotope measurements were obtained by a microdrill device with a dental bit. The various sulfide phases were drilled out of each sample based on BSE mapping results (see Supplementary Materials for drillhole positions). Subsequently, their sulfur isotope compositions were determined using a Thermo Fisher MAT253 continuous flow isotope ratio mass spectrometer coupled to an elemental analyzer (EA-IRMS) at the State Key Laboratory of Ore Deposit Geochemistry, IGCAS in Guiyang with an analytical error of ~0.2‰. Measurements are reported using standard δ-notation relative to the V-CDT international standard. Results were monitored using the International Atomic Energy Agency standards IAEA S1, IAEA S2, and IAEA S3. Their measured $\delta^{34}S$ values (−0.28 ± 0.22‰ (1σ), +22.56 ± 0.21‰ (1σ), and −32.48 ± 0.22‰ (1σ), respectively) conform closely to the published value for each standard (e.g., −0.3‰, +22.62‰, and −32.49‰, respectively; see Supplementary Materials).

4. Results

4.1. Petrographic characteristics

The sediment-hosted Ni-Mo sulfide ores of all three study areas contain both in-situ and reworked sediments (Figs. 2, 4, 6). The in-situ

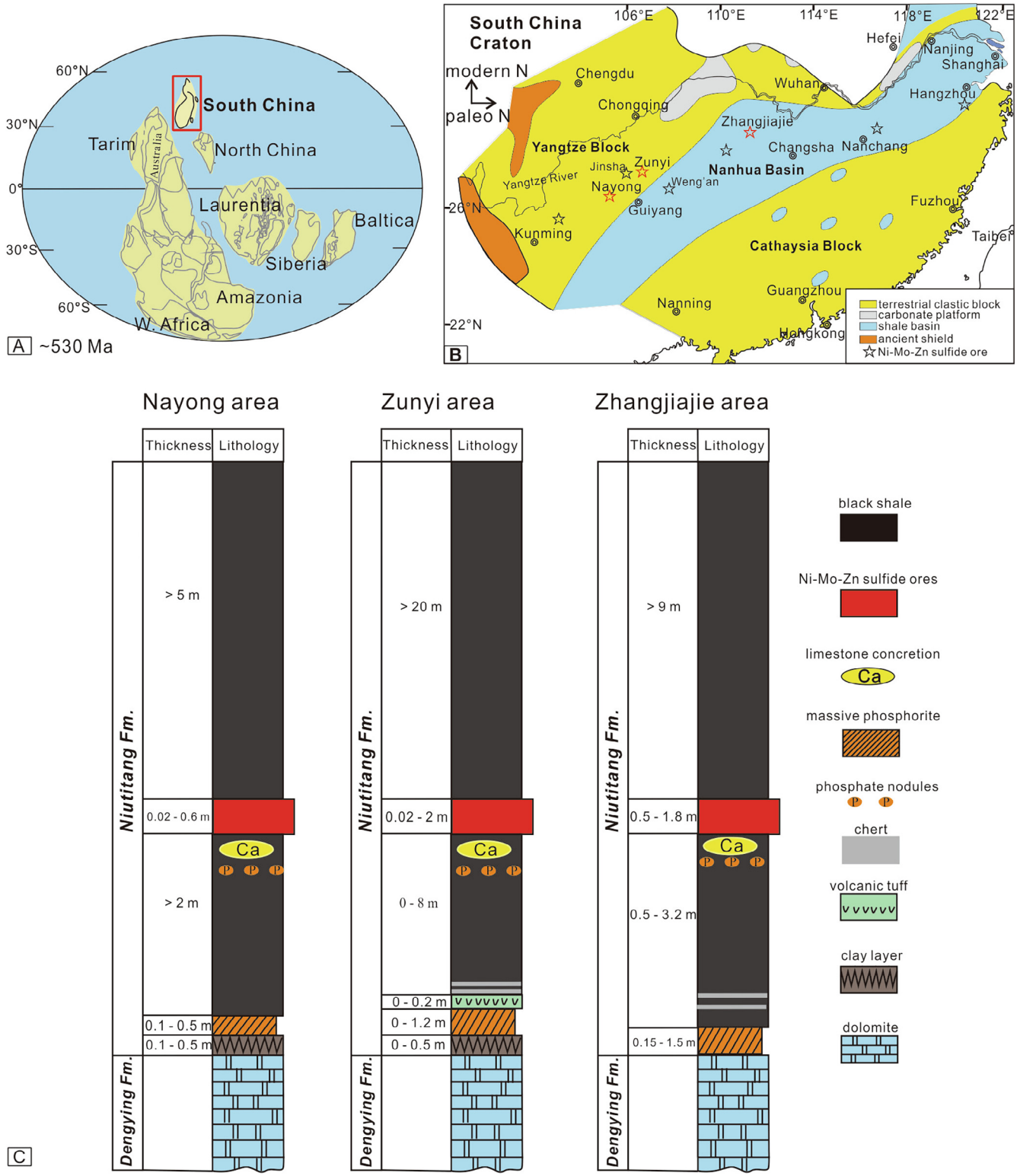

Fig. 1. (A) Early Cambrian global paleogeography (modified from Li et al., 2008). (B) Early Cambrian lithofacies and Ni-Mo sulfide ores of Nanhua Basin, South China (modified from Coveney and Chen, 1991; Feng et al., 2002). (C) Stratigraphic sections of lower Cambrian Niutitang Formation in the Nayong and Zunyi areas of Guizhou Province, and in the Zhangjiajie area of Hunan Province, South China (modified from Li, 1997; Han et al., 2017).

beds are often laminated and contain numerous small grains of pyrite (FeS_2), sphalerite (ZnS), millerite (NiS), gersdorffite (NiAsS), and a MoSC phase along with larger cubic pyrite grains cemented by quartz. In the in-situ beds, sulfides accounts for 85–95% by volume and quartz accounts for 5–15% by volume (Figs. 2, 3C-G, 4, 6). These in-situ deposits completely lack detrital minerals such as illite (Fig. 3C-G). The reworked beds contain abundant oval clasts consisting of sulfides and apatite that they are embedded in a matrix of silicate or phosphate cement (Figs. 2, 3I, L, M, N, 4, 5G, 6). The approximate volumes of quartz, clays, and apatite in these reworked beds are 10–20%, 5–20%, and 5–10%, respectively (Figs. 2, 4, 6). The strong rounding of the oval clasts in the reworked beds suggests downslope transport or strong

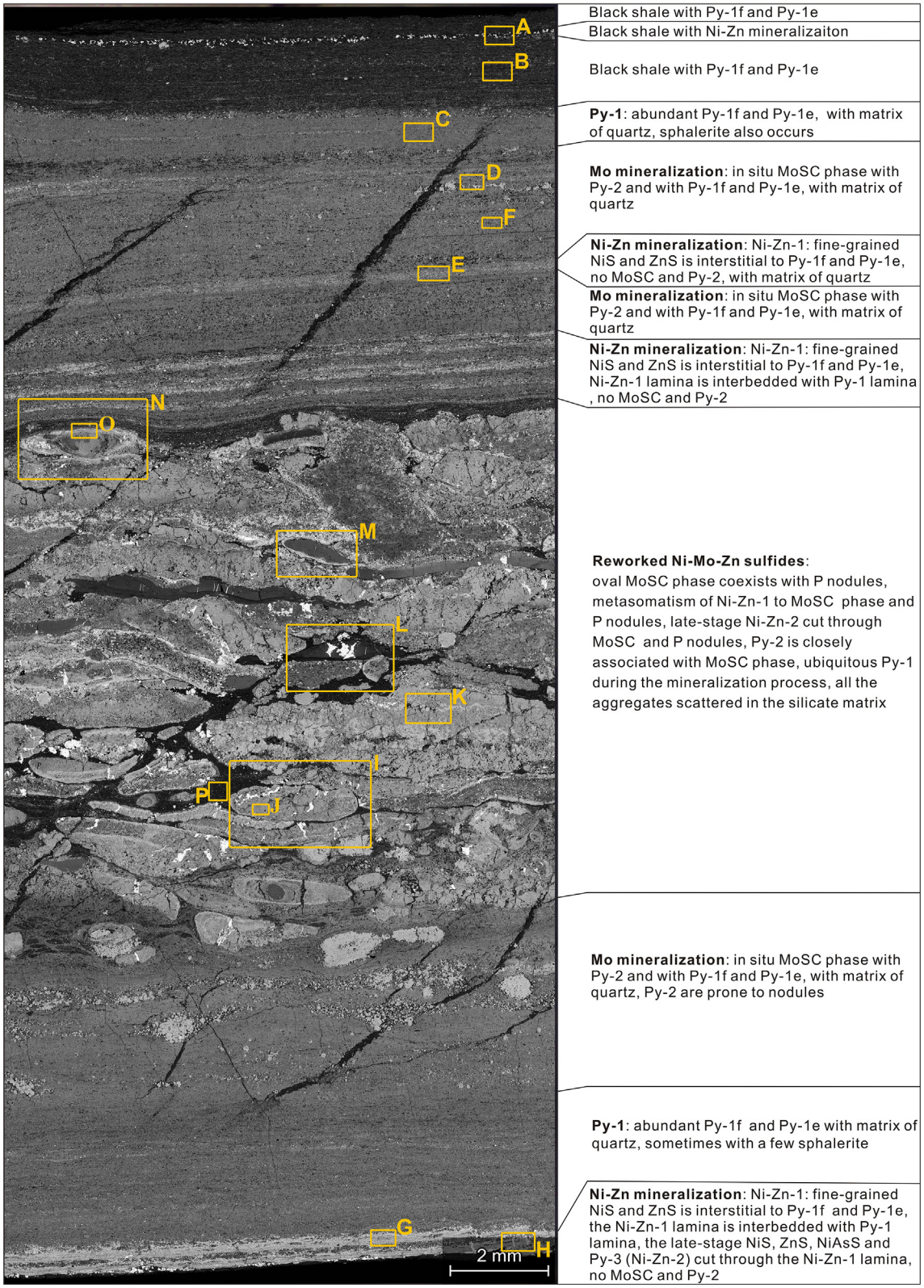

Fig. 2. Backscattered electron (BSE) maps generated using a field emission scanning electron microscope (FESEM) of Ni-Mo sulfide ores from Nayong area, Guizhou Province. In-situ (top and bottom) and reworked (middle) sulfide aggregates and phosphate nodules are present in the silicate matrix. Detailed images of selected areas (A-P) are illustrated in Fig. 3. Abbreviations: Py-1f: fine-grained framboidal pyrites; Py-1e: fine-grained euhedral pyrites; Mo mineralization: MoSC phase and larger pyrite cubes or nodules (Py-2); and Ni-Zn mineralization: intergrown millerite (NiS) and sphalerite (ZnS) with laminated and veined textures.

hydrodynamic conditions. Fractures in the clasts produced by compactional processes were filled with late-stage sulfide precipitates (Fig. 3I, L, M, 5G).

The sulfide ores contain multiple sulfide mineral phases that have a complex paragenetic history (Fig. 7). The main sulfide minerals are a MoSC phase, pyrite (FeS_2), sphalerite (ZnS), millerite (NiS), and

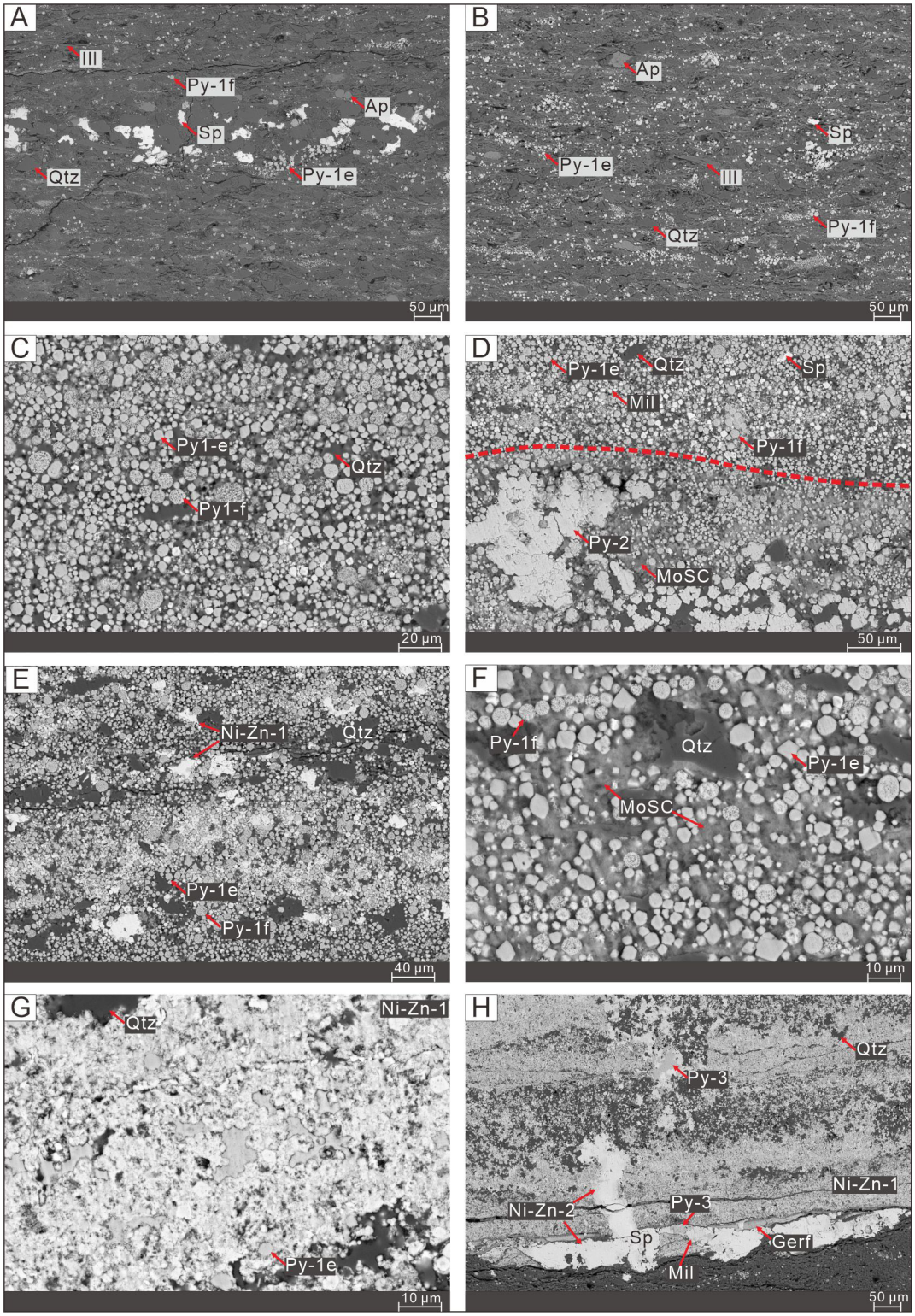

Fig. 3. BSE images for detailed areas of Fig. 2. (A) Black shale with minor framboidal (Py-1f) and euhedral (Py-1e) pyrite and sphalerite (Sp) grains; (B) Black shale with abundant Py-1f and Py-1e; (C) Abundant Py-1f and Py-1e in matrix of quartz (Qtz); (D) Contact of fined-grained Ni-Zn mineralization (Ni-Zn-1, above) and Mo mineralization (MoSC phase) with cubic pyrite and pyrite nodule (Py-2) (below); (E) Laminated Ni-Zn-1, with millerite (Mil) and sphalerite interstitial to Py-1f and Py-1e; (F) In-situ Mo mineralization (MoSC and Py-2), and MoSC phase enclosing some Py-1f and Py-1e; (G) Detailed structure of laminated Ni-Zn-1; (H) Veined Ni-Zn mineralization (Ni-Zn-2) cutting through laminated Ni-Zn-1. Ill = Illite; Ap = apatite; Gerf = gersdorffite. (I) Reworked oval MoSC phase cut through by late-stage sphalerite veinlet (Ni-Zn-2); (J) Oval MoSC phase enclosing some Py-1f and Py-1e; (K) Intergrowth of MoSC phase and Py-2; (L) Phosphate nodule cut through by late-stage sphalerite veinlet (Ni-Zn-2); (M) Metasomatized fine-grained Ni-Zn-1 on the rim of phosphate nodule; (N and O) Metasomatized fine-grained Ni-Zn-1 and MoSC phase on phosphate nodule; (P) Silicate matrix of reworked sulfide aggregates (e.g. MoSC, Py-2, and sphalerite).

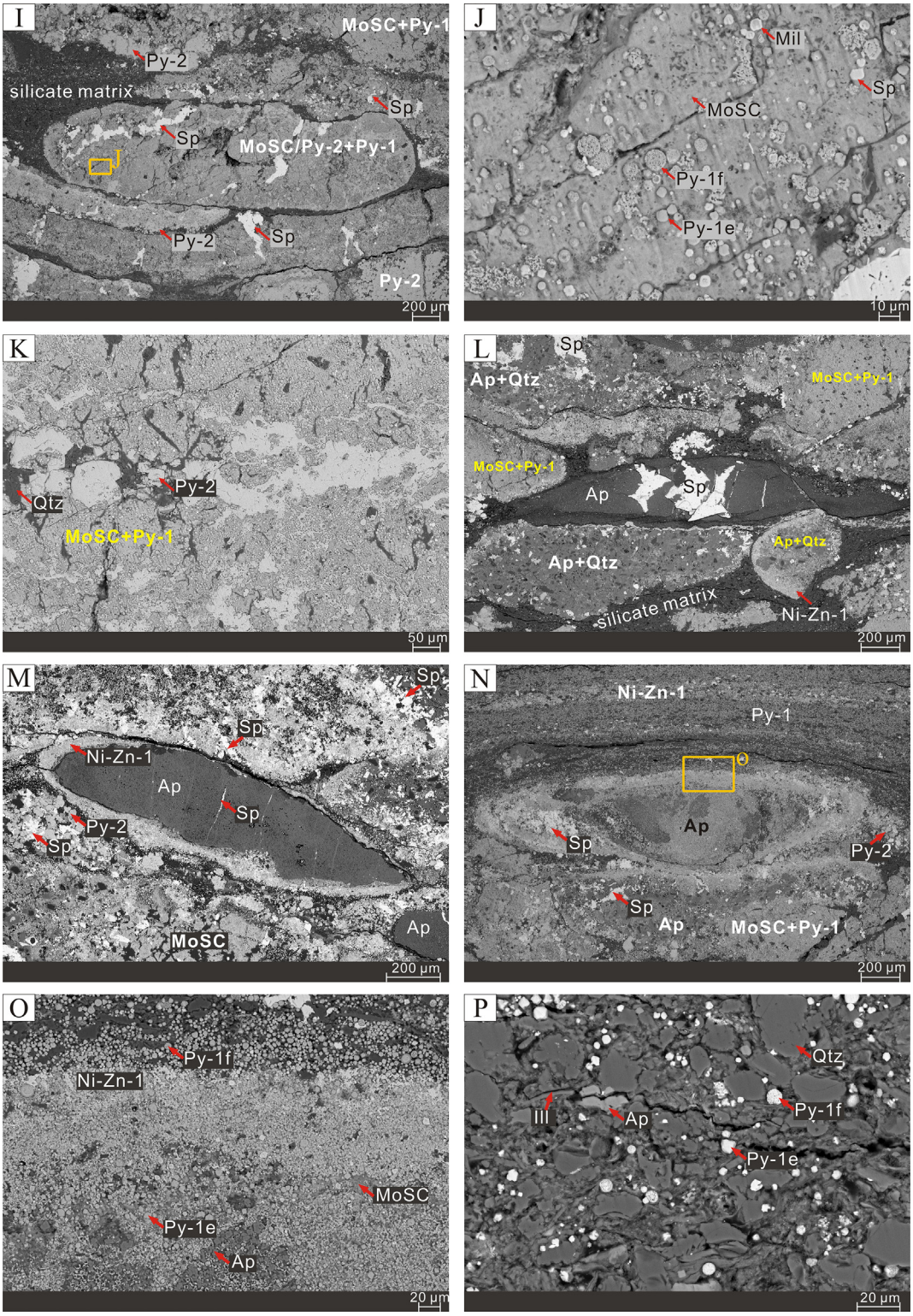

Fig. 3. (*continued*)

gersdorffite (NiAsS) that exhibit a variety of textures. Petrographic examination resulted in identification of three types of pyrite (Py-1, Py-2, Py-3). Py-1 occurs as abundant framboidal (Py-1f) and euhedral (Py-1e) crystals with a mean diameter of < 5 μm (Fig. 3C; Supplementary Materials); it formed throughout the mineralization history of the study units (Figs. 3C-G, 5D). Py-2 occurs as larger cubic pyrite grains (~10–20 μm, Fig. 3D, 5A, 6D) that commonly form nodules (Fig. 3D, 5E, 6B). Py-3 occurs as veins with widths of ~30 μm that are closely associated with veined millerite and sphalerite (Fig. 3H). The estimated volumes of sulfides in the in-situ beds are 10–60% for Py-1, 5–35% for Py-2, and < 1% for Py-3, and the corresponding values for the reworked beds are 10–20% for Py-1, 1–10% for Py-2, and < 1% for Py-3 (Figs. 2, 4, 3H, 6). Nickel and zinc sulfides, comprising 5–10% of both the in-situ and reworked beds, are intimately intergrown but two types (Ni-Zn-1 and Ni-Zn-2) can be distinguished. Ni-Zn-1 occurs mainly as small millerite, gersdorffite and sphalerite grains that are interstitial to

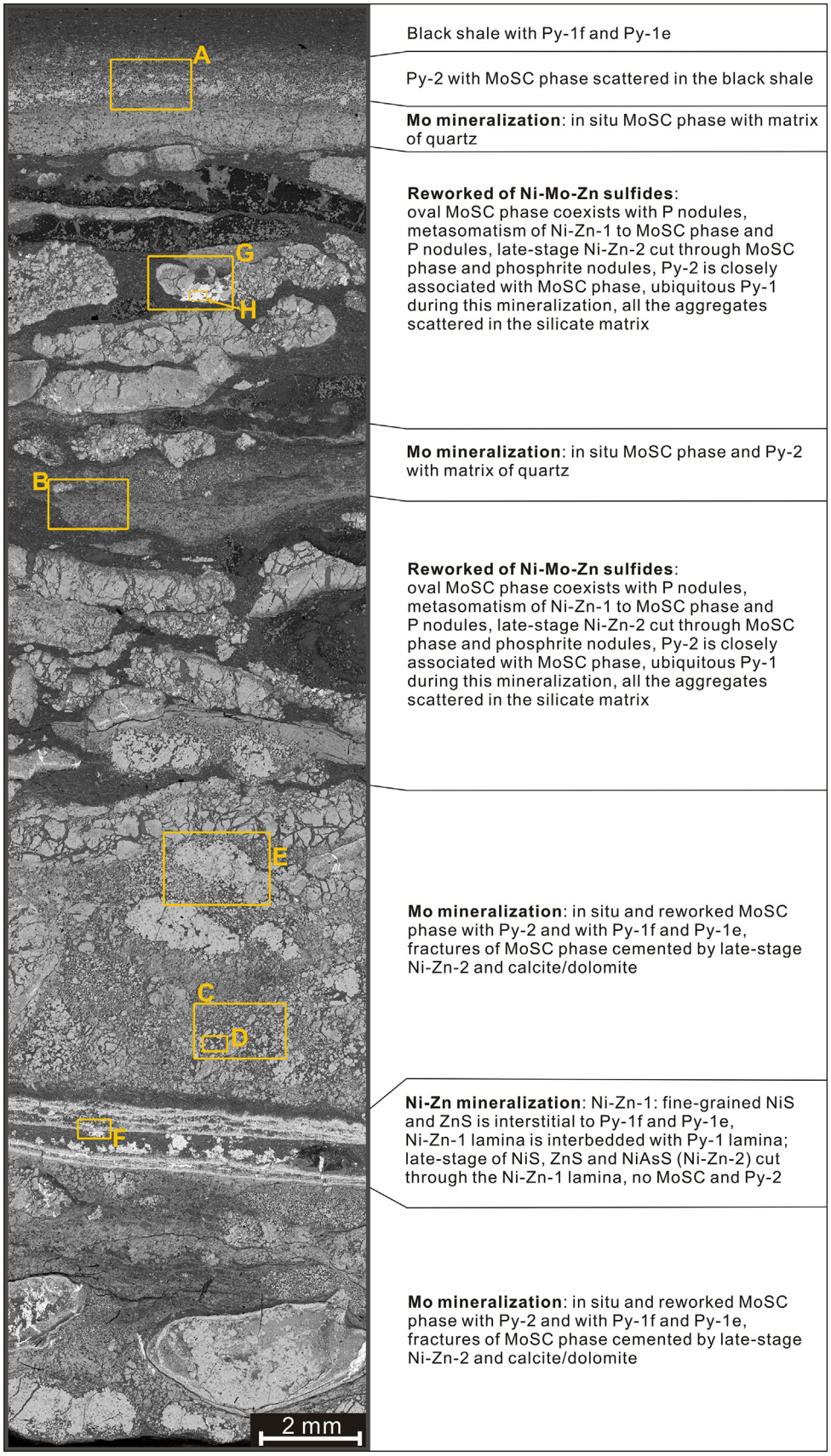

Fig. 4. BSE map of Ni-Mo sulfide ores from Zunyi area, Guizhou Province. A large number of in-situ and reworked sulfide aggregates and phosphate nodules are scattered in the silicate and phosphate matrix. Detailed images of selected areas (A-H) are shown in Fig. 5.

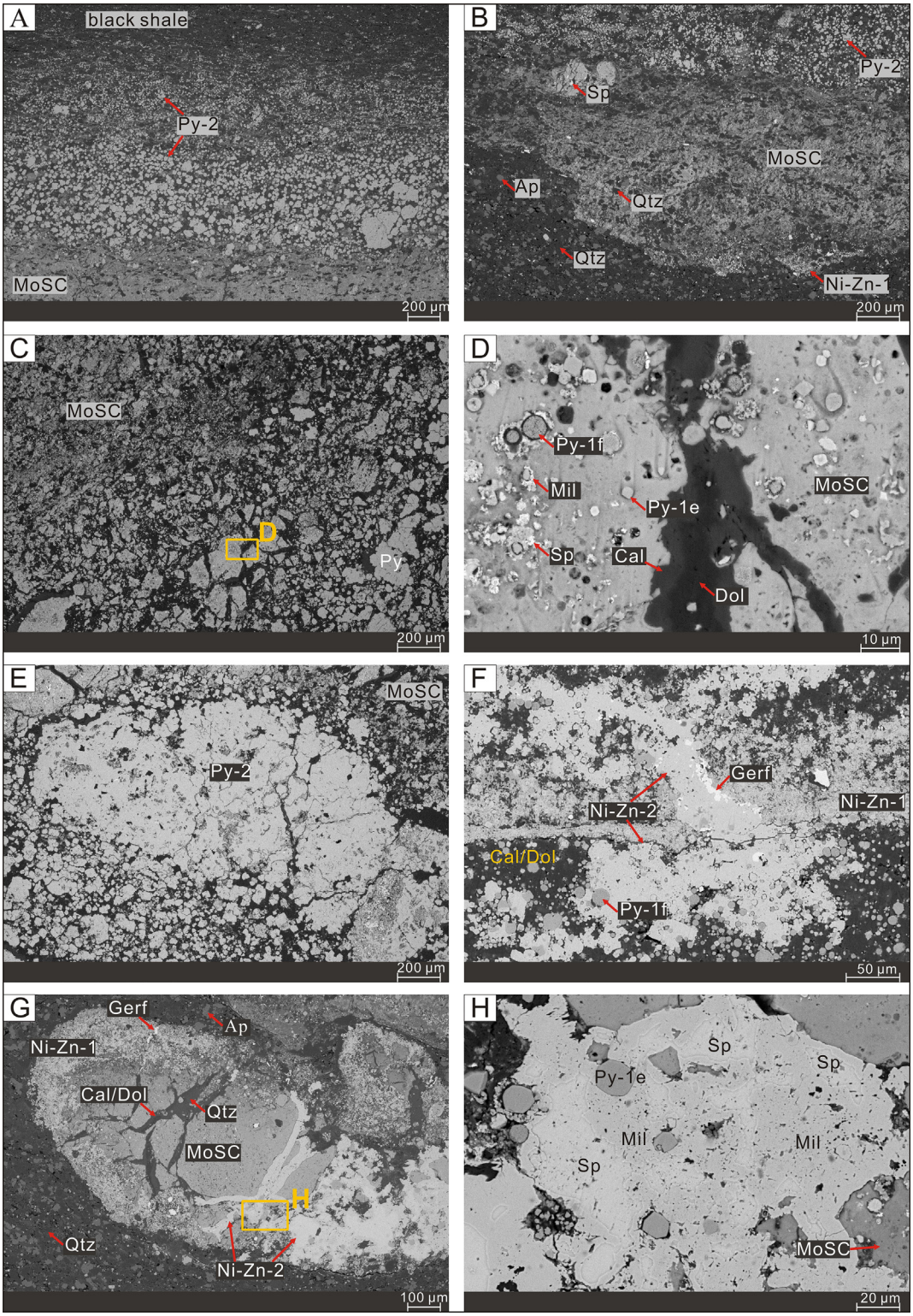

Fig. 5. BSE images for detailed areas of Fig. 4. (A) Contact between black shale and Mo mineralization with Py-2; (B) Re-worked MoSC phase and Py-2 precipitated within the silicate and phosphate matrix; (C) In situ MoSC phase cemented by calcite and dolomite veinlets; (D) Metasomatized fine-grained Ni-Zn-1, Py-1f and Py-1e within the in situ MoSC phase; (E) Cubic pyrite grains around pyrite nodule (Py-2); (F) Fine-grained Ni-Zn-1 cut through by veined Ni-Zn-2; (G) Re-worked oval MoSC phase replaced by fine-grained Ni-Zn-1 and cut through by veined Ni-Zn-2; (H) Intergrown millerite and sphalerite (Ni-Zn-2).

the framboidal and euhedral crystals of Py-1 in laminated (in-situ) deposits (Figs. 3E, G, H, N, 5F). In reworked beds, Ni-Zn-1 type grains occur as metasomatic replacements along the rims of oval clasts (Figs. 3O, 5D, 5G, 6A, 6C). Ni-Zn-2, consisting of millerite, gersdorffite, and sphalerite and associated with Py-3 (Fig. 3H), is a late phase forming veinlets that cut through earlier-formed mineral aggregates (Fig. 3H-I, L, 5F-G). The MoSC phase, comprising 10–60% of the in-situ beds and 30–50% of the reworked beds, occurs in two textural types: in a massive form within in-situ beds (Fig. 3D, 3F, 5C, 6A-B) and as oval clasts within reworked beds (Figs. 3I, 5G). A few framboidal and euhedral pyrite

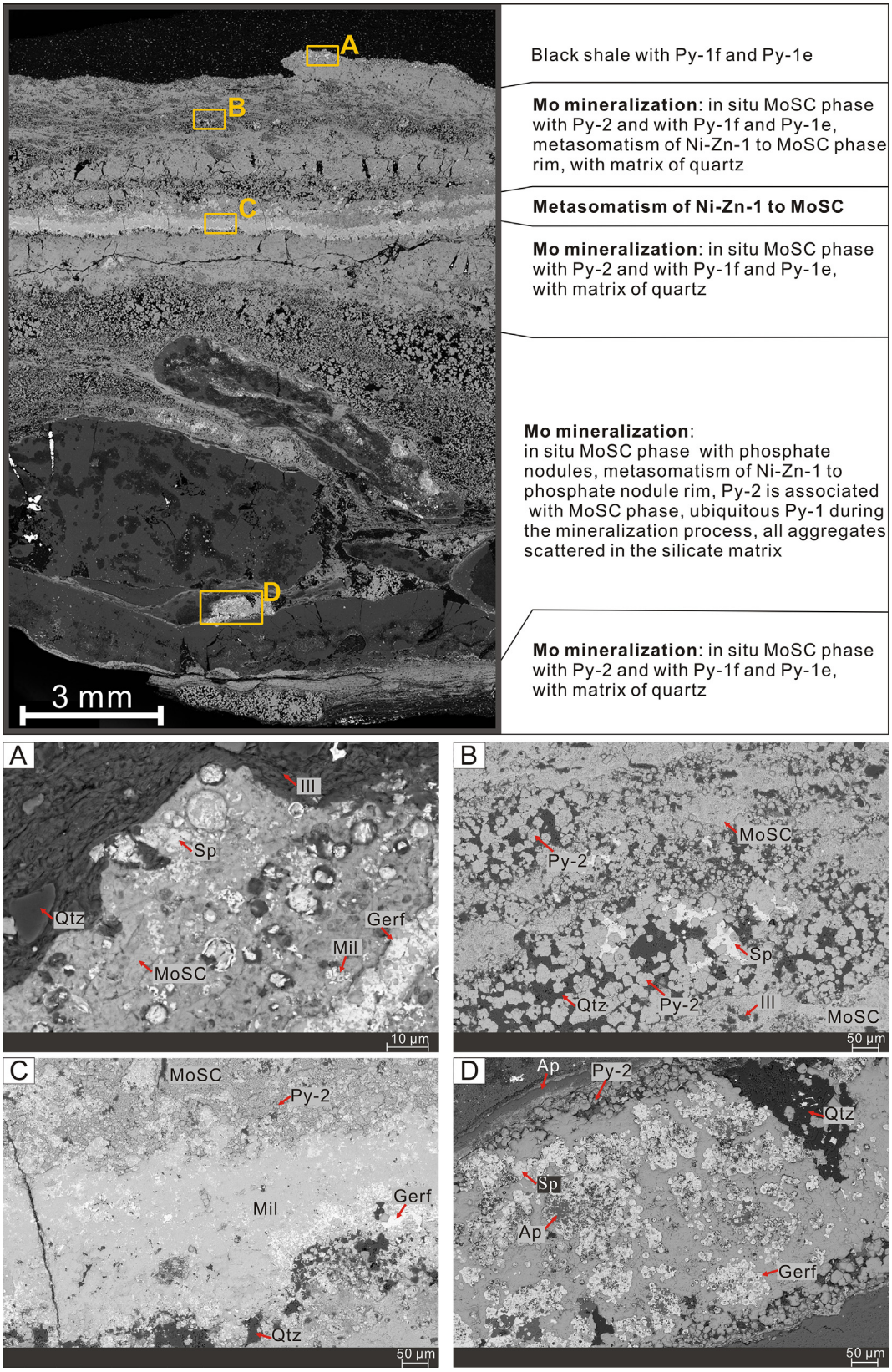

Fig. 6. BSE maps for Ni-Mo sulfide ores from Zhangjiajie area, Hunan Province. Abundant cubic pyrite coexists (Py-1) with the in-situ MoSC phase, along with reworked and phosphate nodules. (A) Rim of MoSC phase replaced by fine-grained Ni-Zn-1; (B) Intergrown MoSC phase and Py-2, with MoSC phase enclosed by Py-1f and Py-1e; (C) Metasomatized fine-grained Ni-Zn-1 and MoSC phase; (D) Py-2 aggregates filled by fine-grained Ni-Zn-1.

Table 1
The sulfur isotope compositions ($\delta^{34}S_{V\text{-}CDT}$/‰) of different sulfide assemblages in the sediment-hosted Ni-Mo sulfide ores in Nayong and Zunyi areas of Guizhou Province and in Zhangjiajie area of Hunan Province, South China.

Sulfides	Nayong area	Zunyi area	Zhangjiajie area
Py-1	−15.7 to +0.01 (−8.4; n = 3)	−1.8 to +1.9 (0.4; n = 3)	–
Py-2	−6.8 (n = 1)	−20.6 to −7.5 (−12.9; n = 17)	−25.1 to −10.8 (−17.0; n = 6)
MoSC	−11.8 to −4.6 (−7.9; n = 6)	−7.2 to +4.4 (−1.3; n = 28)	+8.6 to + 18.7 (+15.5; n = 3)
Ni-Zn-1	−9.1 to −1.7 (−5.3; n = 6)	−2.7 to +8.0 (−2.6; n = 15)	–
Ni-Zn-2	–	−1.8 to −1.0 (−1.35; n = 4)	–

Note: the definitions of sulfides (e.g. Py-1, Py-2, MoSC, Ni-Zn-1 and Ni-Zn-2) are consistent with the text and figures in this study; average values and number of samples are presented in the parentheses. "–" means no data.

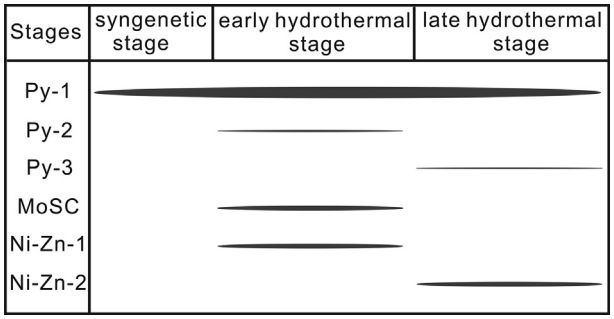

Fig. 7. Simplified paragenetic relationship of Ni-Mo sulfide mineralization. The widths of each sulfide phase represent relative volumes (e.g., with an example of the Nayong sulfide ore in Fig. 2: 40 vol% Py-1, 5 vol% Py-2, < 1 vol% Py-3, 15 vol% MoSC phase, 15 vol% Ni-Zn-1, 15 vol% Ni-Zn-2, and 10 vol% quartz).

grains of type Py-1 are also enclosed by the MoSC phase (Fig. 3J, 5D, 6B), and type Py-2 is always associated with the MoSC phase in both in-situ and reworked beds (Fig. 3D, 5A, 5E, 6B, 6D).

4.2. Sulfur isotope results

All isotopic data generated in this study are given in Table 1 and the Supplementary Materials. The various sulfide phases exhibit $\delta^{34}S$ values ranging from −25.1 to +18.7‰ (Fig. 8, Table 1). For Py-1, $\delta^{34}S$ ranges from −15.7 to +0.01‰ with an average of −8.4‰ in the Nayong area, and from −1.8 to +1.9‰ with an average of +0.4‰ in the Zunyi area. For Py-2, all aggregates and nodules yielded negative $\delta^{34}S$ values, ranging from −20.6 to −6.8‰ with an average of −12.9‰ in the Nayong and Zunyi areas, and from −25.1 to −10.8‰ with an average of −17.0‰ in the Zhangjiajie area. For laminated Ni-Zn-1 phases, $\delta^{34}S$ ranges from −9.1 to −1.7‰ with an average of −5.3‰ in the Nayong area, and from −2.7 to +8.0‰ with an average of +2.6‰ in the Zunyi area. The sulfide aggregates of veined Ni-Zn-2 exhibit slightly negative $\delta^{34}S$ values, ranging from −1.8 to −1.0‰ with an average of −1.4‰ in the Zunyi area. The MoSC phase yields $\delta^{34}S$ ranging from −11.8‰ to −4.6‰ with an average of −7.9‰ in the Nayong area, from −7.2 to +4.4‰ with an average of −1.3‰ in the Zunyi area, and from +8.6 to +18.7‰ with an average of +15.5‰ in the Zhangjiajie area (Fig. 9).

5. Discussion

5.1. Petrographic evidence for synsedimentary Ni-Mo sulfide ores

Petrographic examination yielded a number of observations relevant to the origin of the Ni-Mo sulfide mineralization of the study units. According to our paragenetic analysis, three major mineralization stages can be identified (Fig. 7): (1) Stage 1: syngenetic stage with Py-1 formation throughout the mineralization process, (2) Stage 2: early hydrothermal stage with alternating Mo mineralization (characterized by the MoSC phase and Py-2) and Ni-Zn-1 mineralization (characterized

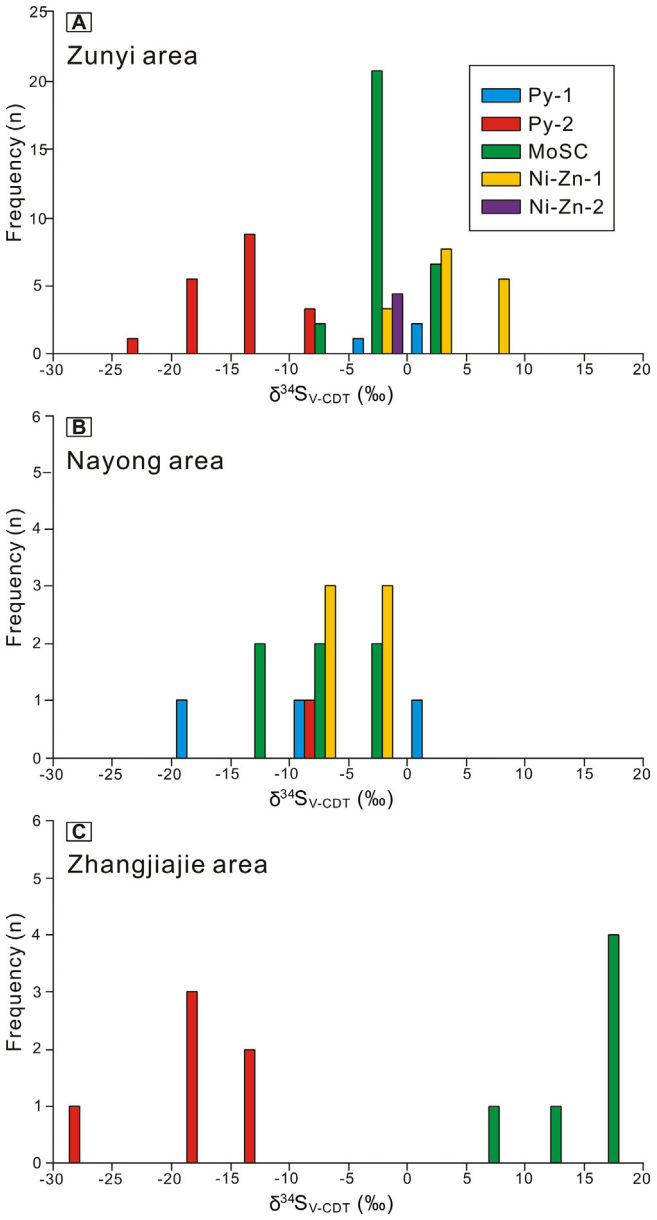

Fig. 8. Histograms of sulfur isotopic composition of the Ni-Mo sulfide ores (e.g., Py-1, Py-2, MoSC, Ni-Zn-1, Ni-Zn-2) from (A) Zunyi area and (B) Nayong area of Guizhou Province, and (C) Zhangjiajie area of Hunan Province.

by fine-grained millerite, gersdorffite, and sphalerite), and (3) Stage 3: late hydrothermal stage with Ni-Zn-2 mineralization (characterized by veined Ni-Zn sulfides and Py-3). In particular, the Mo mineralization and Ni-Zn mineralization alternatively occurred in the in-situ beds with no overlap between them (Fiss. 2, 3D-F). Detailed petrographic

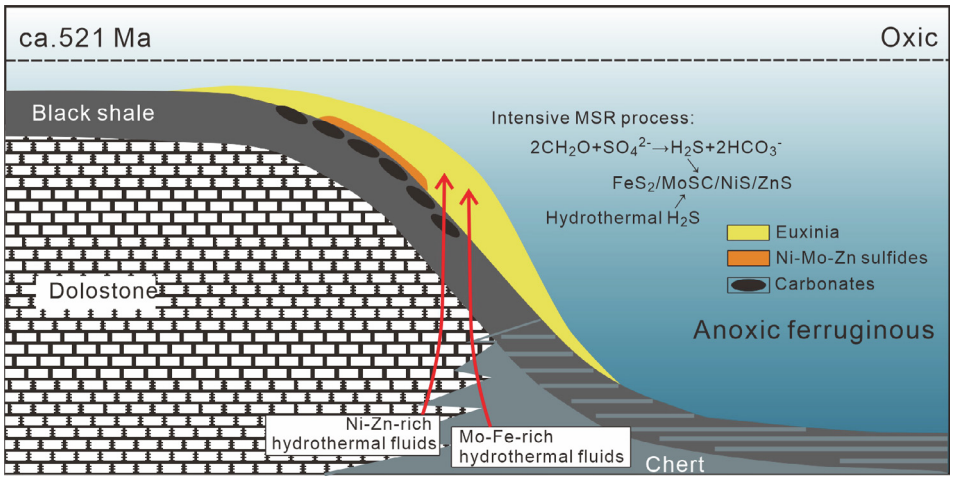

Fig. 9. Model for widespread Ni-Mo sulfide mineralization in early Cambrian (~521 Ma) Nanhua Basin. Ocean stratification with oxic surface waters and ferruginous deep waters are from Feng et al. (2014) and Jin et al. (2016). Intermittent introduction of Mo-Fe-rich or Ni-Zn-rich hydrothermal fluids into the euxinic water column promoted widespread Ni-Mo sulfide mineralization along the southern margin of the Yangtze Platform. Intense microbial sulfate reduction (MSR) also contributed to H_2S in the early Cambrian seawater.

examination demonstrated that this sediment-hosted Ni-Mo sulfide ore had a synsedimentary origin on the basis of the following lines of evidence.

First, Py-1 is mainly composed of abundant fine-grained framboidal and euhedral pyrite crystals having a narrow size distribution (Figs. 3, 5, 6, Supplementary Materials). In the marine environment, precipitation of pyrite in the form of framboids is common under a wide range of water-column redox conditions from suboxic to anoxic/euxinic (Wilkin et al., 1996). The size distribution of pyrite framboids can serve as an effective redox proxy: small pyrite framboids with a narrow size distribution (e.g., mean diameter < 5 μm with standard deviation lower than 2.25 μm) are indicative of syngenetic pyrites formed in the water column in a persistent euxinic (H_2S-bearing) setting (Wilkin et al., 1996; Wignall and Newton, 1998; Bond and Wignall, 2010). However, under suboxic conditions, framboidal pyrite forms mainly in the sediment, where it grows to a larger size (often > 10 μm) and exhibits a more variable size distribution (e.g., standard deviation > 2.5 μm) (Wilkin et al., 1996; Wignall and Newton, 1998; Bond and Wignall, 2010).

In the study samples, fine-grained pyrite crystals are mainly small framboids (i.e., mean diameter of 4.65 μm) exhibiting a narrow size distribution (i.e., standard deviation of 1.65 μm) (Py-1f; Fig. 3C; see Supplementary Materials). These statistics are consistent with most pyrite crystals being of syngenetic origin (i.e., precipitated within a persistently euxinic water column). Redox conditions in early Cambrian seas of South China are known to have been widely anoxic ferruginous to euxinic (Jin et al., 2016; Han et al., 2018), so the Py-1 phase in the present study units was likely precipitated during euxinic episodes in these seas. Given that the Py-1 phase was formed concurrently with all other sulfidic phases during the mineralization sequence of the study units (as shown by petrographic cross-cutting relationships), this demonstrates that most of the sulfide ore is of synsedimentary origin (all except for some late-stage hydrothermal components of Ni-Zn-2; Figs. 3H-I, L, 5F-G). For example, the formation of Py-1 grains commonly occurred in conjunction with the in-situ and reworked MoSC phase (Fig. 3F, J) as well as with Ni-Zn-1 sulfides (Fig. 3E, G). In addition, Mo and Ni-Zn mineralization occurred alternately, as shown by interlayering of thin Mo-rich and Ni-Zn-rich layers (Figs. 2, 3D). The intergrowth of framboids and Ni-Zn sulfides (Fig. 3E, G) and MoSC (Fig. 3F) also suggests that the Ni-Zn sulfides and MoSC phase precipitated concurrently under the same euxinic conditions in which Py-1 formed.

The Ni-Mo sulfide ores were not formed in sediment pore waters during diagenesis because the in-situ beds lack any detrital siliciclastics (Fig. 3C-G). The lack of terrigenous detritus indicates either a sediment-starved system or rapid accumulation of the sulfide ores. The quantity of fine-grained (Py-1) in the sulfide ores (up to 60 vol% of in-situ beds, Fig. 3C) is much greater than that in nearby black shales (< 5 vol%, Fig. 3B, P) but similar to that in stratiform sulfide deposits (e.g., ~50% fine pyrite in the laminated layers of the McArthur River Zn-Pb deposits, Large et al., 2005). It is unlikely that such large amounts of sulfides (e.g., 85–95% vol.% of Ni-Mo-Zn-Fe sulfides in the in-situ beds, Figs. 2, 3C-G, 4, 6) could have precipitated within sediment pore waters during diagenesis. The only silicate mineral in the in-situ beds is chert (~10 vol%), which is intergrown with the sulfide minerals (Fig. 3C) and may have precipitated directly from seawater through the influence of Si-secreting bacteria (Dong et al, 2015). In hydrothermal systems, amorphous silica gels can also easily form from seawater mixed with hydrothermal silica (Westall et al., 2018).

Consequently, these observed textures, especially the ubiquitous framboids and alternating laminae of Mo-rich and Ni-Zn-rich sulfides, indicate that the Ni-Mo sulfide ores had a synsedimentary origin and formed in contact with the overlying water column. This conclusion is also consistent with previous studies in which the sulfide ores were determined to have formed through synsedimentary mineralization processes (Murowchick et al., 1994; Xu et al., 2011).

5.2. Metal sources of the Ni-Mo sulfide ores

The source of Mo in the sulfide layer of the lower Cambrian Niutitang Formation in South China has been debated extensively in earlier studies. The two main hypotheses are a seawater origin (Lehmann et al., 2007; Xu et al., 2013) and a submarine hydrothermal exhalative (SEDEX) origin (Coveney and Chen, 1991; Lott et al., 1999; Jiang et al., 2007a; Han et al., 2017). A seawater origin was proposed on the basis of elemental concentration patterns along with Mo isotope signals, with accumulation occurring in a sediment-starved, stratified basin with a euxinic deep watermass (Lehmann et al., 2007; Xu et al., 2013). However, a seawater source was thought to be unable to explain $\delta^{98/95}$Mo values in the sulfide ores (+1.13 ± 0.14‰) that are lower than those in the black shales hosting them ($\delta^{98/95}$Mo = +1.28 ± 0.41‰) (Jiang et al., 2007b). This observation thus favors a hydrothermal source for Mo mineralization (Jiang et al., 2007b).

Mo mineralization was likely due to injection of Mo-Fe-rich hydrothermal fluids into a euxinic mid-depth watermass. This inference is consistent with the petrographic observations of this study, which show that precipitation of the MoSC phase was decoupled from that of Py-1 grains (Fig. 2). This decoupling between MoSC and Py-1 is incompatible with a seawater origin model. Moreover, the MoSC phase was closely associated with Py-2 grains (Figs. 3D, 5A, 5E, 6B, 6D). The interlamination of the MoSC phase and Py-2 in the in-situ beds reflects high-frequency pulses of Mo-Fe-rich hydrothermal fluids from a submarine vent (Figs. 2 and 4). It should be noted that the oval MoSC phase, Py-2, and apatite nodules with sulfurized rims that are scattered through the reworked beds were the product of downslope transport from a

shallower-water region (Figs. 2, 4, 6).

The Ni-Zn mineralization was associated with emission of hydrothermal fluids into a euxinic mid-depth water layer. This process is characterized by intergrowth of millerite, sphalerite and gersdorffite within Ni-Zn-1 laminae and late-stage Ni-Zn-2 veinlets. In addition, pyrite (Py-3) is found only in small amounts (e.g., < 1 vol%) and is generally associated with Ni-Zn-2 (Fig. 3H). As with Mo mineralization, the decoupled pattern between fine Ni-Zn-1 and Py-1 (Figs. 2 and 4) is inconsistent with a seawater origin for Py-1. Based on the interstitial relationship between Ni-Zn-1 and Py-1 (Fig. 3E, 3G, 3O), we suggest that Ni-Zn-rich hydrothermal fluids were introduced during Py-1 deposition. In addition, the vein interpenetration textures of Ni-Zn-2, which cuts across the Ni-Zn-1 laminae (Figs. 3H, 5F), oval MoSC phase (Fig. 3I, 5G), and apatite nodules (Fig. 3L, M) and Py-2 (Fig. 6D), clearly demonstrate the late-stage hydrothermal fluid origin of Ni-Zn-2.

The Ni-Zn mineralization was related to hydrothermal processes, as shown by various types of geochemical evidence. For instance, positive correlations among the Ni, Pt and Pd contents of the Ni-Mo sulfide ores suggest that Ni and PGE deposition was related to hydrothermalism associated with mafic or ultramafic rocks (Han et al., 2015a,b). Generally, in hydrothermal nickel deposits, the source of nickel is associated with mafic or ultramafic suites (Melekestseva et al., 2013). This conclusion is consistent with the occurrence of mafic and ultramafic rocks in the Proterozoic and lower Paleozoic of South China (Li and Gao, 2000). Given the coexistence of Ni-bearing sulfides and sphalerite, the source of Zn may have been the same hydrothermal fluids that supplied Ni. Experimental study has shown that high-temperature, low-pH, and Cl-rich fluids can be enriched in both Ni and Zn (Marques et al., 2007), providing a metal source for Ni-Zn mineralization.

The petrographic and geochemical lines of evidence discussed above favor a model based on alternating precipitation of Mo and Ni-Zn sulfides related to intermittent emissions of Mo-Fe-rich and Ni-Zn-rich hydrothermal fluids into a euxinic water column, i.e., a sedimentary exhalative (SEDEX) model. Other evidence of hydrothermal activity in the Nanhua Basin during the early Cambrian includes positive Eu anomalies in limestones underlying the Ni-Mo sulfide ores (Han et al., 2017), multi-stage growth of hydrothermal silica chimneys in the black chert successions across the Ediacaran-Cambrian boundary of Hunan Province (Chen et al., 2009), and abundant zoned, euhedral hyalophane in lower Cambrian giant barite ore deposits of Guizhou and Hunan Provinces (Han et al., 2015a,b). The Nanhua Basin sediment-hosted Ni-Mo sulfide ores are similar to shale-hosted massive sulfide deposits of SEDEX origin from the Proterozoic McArthur River Zn-Pb deposit in northern Australia (Large et al., 2005), the Carboniferous Red Dog Zn-Pb deposit in Alaska (Slack et al., 2004), and the Devonian Howard's Pass Zn-Pb deposit in Canada (Gadd et al., 2016, 2017). These shale-hosted massive Zn-Pb deposits were also ascribed to metalliferous fluids vented into the euxinic water column of a restricted sedimentary basin (Slack et al., 2004; Large et al., 2005; Goodfellow, 2007; Gadd et al., 2016, 2017).

5.3. Sulfur sources of the Ni-Mo sulfide ores

Sulfur isotopes can be used to understand biogeochemical sulfur cycling in aqueous systems (Bottrell and Newton, 2006; Lyons et al., 2014; Fike et al., 2015). The dissimilatory microbial sulfate reduction (MSR) process plays a pivotal role in sulfur isotope fractionation in Earth surface environments. During the MSR process, sulfate (e.g., the electron acceptor) is reduced by organic materials (e.g., the electron donors), e.g., $SO_4^{2-} + 2CH_2O \rightarrow H_2S + 2HCO_3^-$ (Sim et al., 2011; Bradley et al., 2016). The generated hydrogen sulfide (H_2S) is preferentially enriched in ^{32}S and readily precipitates as metal sulfides (e.g., pyrite), while the residual sulfate becomes isotopically enriched in ^{34}S (Thode et al., 1951; Habicht and Canfield, 2001; Bradley et al., 2016; Sim et al., 2017). The MSR process yields a large range of sulfur isotope fractionations (up to ~70‰) (Brunner and Bernasconi, 2005; Canfield et al., 2010; Sim et al., 2011) as a function of various physiological and environmental factors, including cell-specific sulfate reduction rate (csSRR), the availability and type of organic compounds, and sulfate concentration and temperature (Habicht et al., 2002; Hoek et al., 2006; Sim et al., 2011, 2017; Leavitt et al., 2013; Bradley et al., 2016). For instance, an inverse correlation between the magnitude of sulfur isotope fractionation and csSRR has been observed in experimental studies (Leavitt et al., 2013; Sim et al., 2011, 2017; Antler et al., 2017). Sulfur isotope fractionation is also closely related to the types and amounts of organic materials as electron donors. Lesser amounts of organic material usually yield large sulfur isotope fractionations (Sim et al., 2011; Leavitt et al., 2013; Bradley et al., 2016). Higher sulfate concentrations also promote larger sulfur isotope fractionations (Habicht et al., 2002), although low sulfate environments can yield large fractionations if the electron donors limit sulfate reduction rates early in the MSR process (Gomes and Hurtgen, 2013, 2015; Crowe et al., 2014). Also, moderate temperatures (~ < 40 °C) are usually suitable for producing large fractionations, but smaller fractionations occur at increasingly higher temperatures (e.g., 40–60 °C) (Hoek et al., 2006). The influence of environmental factors on sulfur isotope fractionation is intrinsically related to the csSRR. Biological sulfur isotope fractionations are related to relative rates of sulfate exchange across the membrane versus intracellular sulfate reduction (Sim et al., 2017). The sources of reduced sulfur of Ni-Mo sulfide ores are discussed below based on these principles in the context of our petrographic results and sulfur isotope data.

The sulfur source for fine-grained Py-1 phase was biogenic H_2S in early Cambrian seawater, as can be inferred from the variable range of $\delta^{34}S$ values, i.e., from −1.8 to +1. 9‰ in the Zunyi area, and from −15.7 to 0.0‰ in the Nayong area (Fig. 8, Table 1, Supplementary Materials). The fine-grained Py-1 formed via direct precipitation from ferrous ion (Fe^{2+}) in the presence of free H_2S in seawater. Given an early Cambrian seawater sulfate $\delta^{34}S$ of +33 ± 5‰ (Kampschulte and Strauss, 2004), these Py-1 $\delta^{34}S$ values are equivalent to fractionations of +31 to +49‰ relative to seawater sulfate, a range that is consistent with a biogenic H_2S source generated by the MSR process (Brunner and Bernasconi, 2005; Canfield et al., 2010; Sim et al., 2011). Formation of Py-1 throughout the mineralization process with large sulfur isotope fractionations (e.g., up to +49%) suggests that intense MSR and euxinic conditions prevailed during Ni-Mo sulfide mineralization.

The sulfur sources for the MoSC and Py-2 phases probably included both biogenic H_2S in early Cambrian seawater and hydrothermal H_2S emanating from exhalative submarine vents. Petrographic observations reveal an intimate intergrowth between the MoSC and Py-2 phases, but the sulfur isotope compositions of these two phases vary greatly. The average $\delta^{34}S$ of the MoSC phase is highly variable, i.e., −7.9‰ in the Nayong area, −1.3‰ in the Zunyi area, and +15.5‰ in the Zhangjiajie area, whereas the Py-2 phase in all three areas has uniformly negative $\delta^{34}S_{Py\text{-}2}$ values, i.e., −6.8‰ in the Nayong area, −12.9‰ in the Zunyi area, and −17.0‰ in the Zhangjiajie area (Fig. 8, Table 1; Supplementary Materials). Mo-Fe-rich hydrothermal fluids are commonly generated during the magmatic-hydrothermal evolution of granite, yielding sulfides with a narrow range of $\delta^{34}S$ values (−5 to +5‰; Leng et al., 2018). However, a wide range of $\delta^{34}S$ values for the MoSC and Py-2 phases (e.g., −25.1 to +18.7‰; Fig. 8, Table 1; Supplementary Materials) is inconsistent with those of sulfides derived from Mo-Fe-rich hydrothermal fluids (e.g., −5 to +5‰; Leng et al., 2018), even though hydrothermal H_2S was a major source of sulfur. Both higher (to +18.7‰) and lower values (to −25.1‰) are consistent with biogenic H_2S generated through MSR processes. A similar range of $\delta^{34}S$ variation (from −26 to +22‰) for pyrite nodules based on SHRIMP analysis was also ascribed to biogenic reduction of seawater sulfate in an anoxic basin (Murowchick et al., 1994). It should be noted that the sulfate reduction process can occur either in the seawater column or in marine sediments, producing a large range of sulfur isotope fractionations (Magnall et al., 2016, 2020; Johnson et al.,

2018; Jørgensen et al., 2019). As discussed above, given that precipitation of the Mo-Fe sulfides required hydrothermal inputs into a euxinic water column, the Mo-Fe sulfides were syngenetic and not likely formed during diagenesis. Therefore, the sulfur for Mo mineralization in the Nayong and Zunyi areas may have been derived from both biogenic and hydrothermal H_2S in early Cambrian seawater. However, neither the high $\delta^{34}S$ values of MoSC (+8.6 to +18.7‰) nor the low $\delta^{34}S$ values of Py-2 (−25.1 to −10.8‰) in the Zhangjiajie area are consistent with a magmatic source, so both were likely derived from biogenic H_2S generated by MSR.

The sulfur source for Ni-Zn mineralization was mainly derived from hydrothermal H_2S by emissions. Petrographic relationships clearly show that the Ni-Zn-1 sulfides were precipitated during Py-1 formation (Fig. 3E, 3G, 3O, 5F). The sulfur isotope values of Ni-Zn-1 range from −9.1 to −1.7‰ and from −2.7 to +8.0‰ in the Nayong and Zunyi areas, respectively (Fig. 8, Table 1; Supplementary Materials). In addition, the veined Ni-Zn-2 exhibits $\delta^{34}S$ values from −1.8 to −1.0‰, within the range of $\delta^{34}S$ values for Ni-Zn-1 (Fig. 8). If the Ni and Zn originated from hydrothermal processes related to ultramafic or mafic rocks, then the H_2S was probably also derived from hydrothermal fluids. In ultramafic- or mafic-hosted seafloor hydrothermal systems, sulfides generally exhibit slightly elevated $\delta^{34}S$ values (+3.7‰ to +12.7‰) owing to the interaction of seawater with basement rocks (e.g., basalt and peridotite) at high temperatures, i.e., through TSR processes (Alt and Shanks, 2003; Alt et al., 2012; Zeng et al., 2017). Although TSR tends to yield positive $\delta^{34}S$ values, fluid interaction with sediments or SO_2 disproportionation can result in ^{34}S-depleted H_2S (e.g., to −5.5‰; Peter and Shanks, 1992; McDermott et al., 2015). Hence, the limited $\delta^{34}S$ range (Fig. 8) and mostly positive $\delta^{34}S$ values of the Ni-Zn sulfides (+0.2 to +8.0‰, Supplementary Materials) suggest that sulfur was mainly derived from hydrothermal fluids during Ni-Zn mineralization.

In summary, we suggest that biogenic H_2S derived from seawater sulfate through the MSR process and hydrothermal H_2S both contributed to the formation the Ni-Mo sulfide ores of the basal Niutitang Formation, although their proportions varied in different areas of the Nanhua Basin. Based on petrographic observations, the metallogensis model of the Niutitang Ni-Mo sulfide ores was similar to that of SEDEX deposits, and the sulfur isotope evidence supports a sulfur fractionation mechanism and source of Ni-Mo sulfide ores consistent with shale-hosted Zn-Pb SEDEX deposits (Goodfellow, 1987; Leach et al., 2005). Based on this, the distribution of $\delta^{34}S$ values between Ni-Mo-Zn sulfide ores (−25.1 to +18.7‰) is consistent with those shale-hosted SEDEX Zn-Pb deposits overlapped partially (e.g., −5 to +15‰; Leach et al., 2005).

5.4. Implications for early Cambrian marine systems of South China

Sediment-hosted Ni-Mo sulfide mineralization is likely to have affected the marine sulfur cycle of the Nanhua Basin during the early Cambrian. Our isotopic data suggest that a fraction of the sulfide sulfur was derived from H_2S produced through microbial sulfate reduction (MSR). Early Cambrian seawater sulfate concentrations are thought to have been > 3 mM based on fluid inclusion data and global model calculations (Horita et al., 2002; Lowenstein et al., 2003; Brennan et al., 2004; Algeo et al., 2015). However, the pyrite sulfur isotope compositions of black shales in South China indicate a minimal seawater sulfate content for Neoproterozoic and Cambrian seas (Feng et al., 2014; Jin et al., 2016), suggesting that extensive sulfide mineralization in the early Cambrian Nanhua Basin occurred in the context of a small oceanic sulfate reservoir. Correlations of lower Cambrian strata in South China indicate that widespread Ni-Mo sulfide mineralization (521 ± 5 Ma, Xu et al., 2011) coincided with an interval of low seawater sulfate concentrations (~529–514 Ma; Feng et al., 2014; Jin et al., 2016).

A subset of sulfur isotope values from the present study units falls outside of the well-defined mode at −9 to +8‰ that represents hydrothermal emissions of H_2S. These values, which range from −25.1‰ at the low end to +18.7‰ at the high end (Fig. 8, Table 1), are likely to have been generated through MSR of seawater sulfate mediated by Rayleigh distillation. The sulfur isotopic composition of Cambrian seawater sulfate was +33.5 ± 5‰ based on the $\delta^{34}S$ of carbonate-associated sulfate (CAS) (Kampschulte and Strauss, 2004). Relative to this value, the observed range of sulfide $\delta^{34}S$ values in the study units (−25.1 to +18.7‰) represents $\Delta^{34}S_{sulfate\text{-}sulfide}$ of ~14 to +58‰, which is consistent with microbial fractionation under conditions of variable seawater sulfate concentrations (Thode et al., 1951; Brunner and Bernasconi, 2005; Sim et al., 2011; Algeo et al., 2015). In the context of the restricted Nanhua Basin (Lehmann et al., 2016), the wide range of MSR fractionation may have been due to strong local variation of seawater sulfate concentrations within the early Cambrian Nanhua Basin, which would have been generally low but locally augmented by oxidation of hydrothermally emitted H_2S. SEDEX ore precipitation was thus important in modulating seawater chemistry within the early Cambrian Nanhua Basin.

A redox-stratified ocean, characterized by coexisting oxic surface waters, ferruginous deep-waters and intermittently euxinic mid-depth waters, prevailed in the Nanhua Basin during the early Cambrian and may have been inherited from late Proterozoic marine systems (Li et al., 2010; Feng et al., 2014; Jin et al., 2016; Zhao et al., 2019). Changes in redox states and seawater chemistry from the late Ediacaran to early Cambrian may also have had an important effect on the diversity of mineralized skeletal organisms (e.g., small shelly fauna and the Chengjiang Biota; Zhao et al., 2018). This study suggests that large-scale H_2S emissions to seawater occurred in the Nanhua Basin around 521 Ma. This conclusion is consistent with that of Wille et al. (2008), who used Mo isotope data to infer intense upwelling of H_2S-rich deep waters during the early Cambrian. This scenario, in which deep basinal waters of the early Cambrian Nanhua Basin were strongly euxinic, would have been a limiting factor on the expansion of early marine animal life into deeper basinal habitats, and it had the potential to create episodic biotic stresses in shallow-water areas through upwelling of toxic H_2S or chemocline-upward excursions (e.g., Kump et al., 2005).

6. Conclusions

Petrographic characteristics and sulfur isotopic composition of SEDEX ores in the early Cambrian Nanhua Basin reveal multiple sulfide phases with a variety of textures and characteristic $\delta^{34}S$ patterns. Abundant framboidal and euhedral pyrites (Py-1) that formed throughout the whole mineralization process resulted from the interaction of ferruginous seawater with biogenic H_2S derived from the MSR process. The intimate intergrowth of a MoSC phase with pyrite cubes or nodular (Py-2) (Mo mineralization) was linked to intermittent pulses of Mo-Fe-bearing hydrothermal fluids. Both hydrothermal and biogenic H_2S contributed to coeval precipitation of MoSC and Py-2 phases in the Nayong and Zunyi areas, whereas biogenic H_2S was responsible for MoSC and Py-2 phases in the Zhangjiajie area. The Ni-Zn mineralization was closely associated with the Ni-Zn-bearing hydrothermal fluid with H_2S associated with hydrothermal vents. Both hydrothermal H_2S and biogenic H_2S were present in Nanhua Basin seawater during the early Cambrian, and significantly contributed to Ni-Mo sulfide mineralization. The presence of euxinic deep waters in this basin was a limiting factor on the expansion of early marine animal life into deep-water habitats.

Declaration of Competing Interest

The authors declare that they have no known competing financial interests or personal relationships that could have appeared to influence the work reported in this paper.

Acknowledgments

This study was funded by the Strategic Priority Research Program (B) of Chinese Academy of Sciences (XDB18000000) and the National Natural Science Foundation of China (41890841, 41873056, 41673053, U1812402). We give many thanks to Dr. Jing Gu for determining the sulfur isotope compositions, to Drs. Hao Yan, Youqiang Qi, Chengbiao Leng, Qi Liu and Chengsheng Jin for discussing the sulfur isotope fractionation, the paragenesis and the hydrothermal process, and to reviewers for evaluation and improvement of the manuscript.

Appendix A. Supplementary data

Supplementary data to this article can be found online at https://doi.org/10.1016/j.precamres.2020.105757.

References

Algeo, T.J., Luo, G.M., Song, H.Y., Lyons, T.W., Canfield, D.E., 2015. Reconstruction of secular variation in seawater sulfate concentrations. Biogeosciences 12, 2131–2151.
Alt, J.C., Shanks, W.C., 2003. Serpentinization of abyssal peridotites from the mark area, mid-Atlantic ridge: sulfur geochemistry and reaction modeling. Geochim. Cosmochim. Acta 67, 641–653.
Alt, J.C., Shanks, W.C., Crispini, L., Gaggero, L., Schwarzenbach, E.M., FrühGreen, G.L., Bernasconi, S.M., 2012. Uptake of carbon and sulfur during seafloor serpentinization and the effects of subduction metamorphism in Ligurian peridotites. Chem. Geol. 322–323, 268–277.
Antler, G., Turchyn, A.V., Ono, S., Sivan, O., Bosak, T., 2017. Combined ^{34}S, ^{33}S and ^{18}O isotope fractionations record different intracellular steps of microbial sulfate reduction. Geochim. Cosmochim. Acta 203, 364–380.
Bond, D.P.G., Wignall, P.B., 2010. Pyrite framboid study of marine Permian-Triassic boundary sections: a complex anoxic event and its relationship to contemporaneous mass extinction. Geol. Soc. Am. Bull. 122, 1265–1279.
Bottrell, S., Newton, R.J., 2006. Reconstruction of changes in global sulfur cycling from marine sulfate isotopes. Earth-Sci. Rev. 75, 59–83.
Bradley, A.S., Leavitt, W.D., Schmidt, M., Knoll, A.H., Girguis, P.R., Johnston, D.T., 2016. Patterns of sulfur isotope fractionation during microbial sulfate reduction. Geobiology 14, 91–101.
Brennan, S.T., Lowenstein, T.K., Horita, J., 2004. Seawater chemistry and the advent of biocalcification. Geology 32, 473–476.
Brunner, B., Bernasconi, S.M., 2005. A revised isotope fractionation model for dissimilatory sulfate reduction in sulfate reducing bacteria. Geochim. Cosmochim. Acta 69, 4759–4771.
Canfield, D.E., Farquhar, J., Zerkle, A.L., 2010. High isotope fractionations during sulfate reduction in a low-sulfate euxinic ocean analog. Geology 38, 415–418.
Cao, J., Hu, K., Zhou, J., Shi, C.H., Bian, L.Z., Yao, S.P., 2013. Organic clots and their differential accumulation of Ni and Mo within early Cambrian black-shale hosted polymetallic Ni–Mo deposits, Zunyi, South China. J. Asian Earth Sci. 62, 531–536.
Chen, D.Z., Wang, J.G., Qing, H.R., Yan, D.T., Li, R.W., 2009. Hydrothermal venting activities in the Early Cambrian, South China: petrological, geochronological and stable isotopic constraints. Chem. Geol. 258, 168–181.
Chen, D.Z., Zhou, X.Q., Fu, Y., Wang, J.G., Yan, D.T., 2015. New U-Pb zircon ages of the Ediacaran-Cambrian boundary strata in South China. Terra Nova 27, 62–68.
Clark, S.H.B., Poole, F.G., Wang, Z., 2004. Comparison of some sediment-hosted, stratiform barite deposits in China, the United States, and India. Ore Geol. Rev. 24, 85–101.
Coveney Jr., R.M., Chen, N.S., 1991. Ni–Mo–PGE–Au-rich ores in Chinese black shales and speculations on possible analogues in the United States. Mineral. Deposita 26, 83–88.
Crowe, S.A., Paris, G., Katsev, S., Jones, C.A., Kim, S.T., Zerkle, A.L., Nomosatryo, S., Fowle, D.A., Adkins, J.F., Sessions, A.L., Farquhar, J., Canfield, D.E., 2014. Sulfate was a trace constituent of Archean seawater. Science 346, 735–739.
Dong, L., Shen, B., Lee, C.T.A., Shu, X.J., Peng, Y., Su, Y., Tang, Z., Rong, H., Lang, X., Ma, H., Yang, F., Guo, W., 2015. Germanium/silicon of the Ediacaran-Cambrian Laobao cherts: implications for the bedded chert formation and paleoenvironment interpretations. Geochem. Geophy. Geosy. 16, 751–763.
Feng, L.J., Li, C., Huang, J., Chang, H.J., Chu, X.L., 2014. A sulfate control on marine mid-depth euxinia on the Early Cambrian (ca. 529–521 Ma) Yangtze Platform, South China. Precambrian Res. 246, 123–133.
Feng, Z.Z., Peng, Y.M., Jin, Z.K., Bao, Z.D., 2002. Lithofacies palaeogeography of the early Cambrian in China. J. Palaeogeogr. 4, 1–14 (in Chinese with English abstract).
Fike, D.A., Grotzinger, J.P., 2008. A paired sulfate–pyrite $\delta^{34}S$ approach to understanding the evolution of the Ediacaran-Cambrian sulfur cycle. Geochim. Cosmochim. Acta 72, 2636–2648.
Fike, D.A., Bradley, A.S., Rose, C.V., 2015. Rethinking the ancient sulfur cycle. Annu. Rev. Earth Planet. Sci. 43, 593–622.
Gadd, M.G., Layton-Matthews, D., Peter, J.M., Paradis, S., 2016. The world-class Howard's Pass SEDEX Zn-Pb district, Selwyn Basin, Yukon. Part I: trace element compositions of pyrite record input of hydrothermal, diagenetic, and metamorphic fluids to mineralization. Mineral. Deposita 51, 319–342.
Gadd, M.G., Layton-Matthews, D., Peter, J.M., Paradis, S., Jonasson, I.R., 2017. The world-class Howard's Pass SEDEX Zn-Pb district, Selwyn Basin, Yukon. Part II: the roles of thermochemical and bacterial sulfate reduction in metal fixation. Mineral. Deposita 52, 405–419.
Goldberg, T., Strauss, H., Guo, Q.J., Liu, C.Q., 2007. Reconstructing marine redox conditions for the Early Cambrian Yangtze Platform: evidence from biogenic sulphur and organic carbon isotopes. Palaeogeogr. Palaeoclimatol. Palaeoecol. 254, 175–193.
Gomes, M.L., Hurtgen, M.T., 2013. Sulfur isotope systematics of a euxinic, low-sulfate lake: evaluating the importance of the reservoir effect in modern and ancient oceans. Geology 41, 663–666.
Gomes, M.L., Hurtgen, M.T., 2015. Sulfur isotope fractionation in modern euxinic systems: implications for paleoenvironmental reconstructions of paired sulfate–sulfide isotope records. Geochim. Cosmochim. Acta 157, 39–55.
Goodfellow, W.D., 1987. Anoxic stratified oceans as a source of sulphur in sediment-hosted stratiform Zn-Pb deposits (Selwyn basin, Yukon, Canada). Chem. Geol. 65, 359–382.
Goodfellow W.D., 2007. Base metal metallogeny of the Selwyn Basin, Canada. In: Goodfellow, W.D., (ed.), Mineral Deposits of Canada: A Synthesis of Major Deposit-Types, District Metallogeny, the Evolution of Geological Provinces, and Exploration Methods: Geological Association of Canada Mineral Deposits Division Special Publication 5, pp. 553–579.
Habicht, K.S., Canfield, D.E., 2001. Isotope fractionation by sulfate-reducing natural populations and the isotopic composition of sulfide in marine sediments. Geology 29, 555–558.
Habicht, K.S., Gade, M., Thamdrup, B., Berg, P., Canfield, D.E., 2002. Calibration of sulfate levels in the Archean ocean. Science 298, 2372–2374.
Halevy, I., Peters, S.E., Fischer, W.W., 2012. Sulfate burial constraints on the Phanerozoic sulfur cycle. Science 337, 331–334.
Horita, J., Zimmermann, H., Holland, H.D., 2002. Chemical evolution of seawater during the Phanerozoic. Geochim. Cosmochim. Acta 66, 3733–3756.
Han, S., Hu, K., Cao, J., Pan, J., Xia, F., Wu, W., 2015a. Origin of early Cambrian black-shale-hosted barite deposits in South China: mineralogical and geochemical studies. J. Asian Earth Sci. 106, 79–94.
Han, T., Zhu, X.Q., Li, K., Jiang, L., Zhao, C.H., Wang, Z.G., 2015b. Metal sources for the polymetallic Ni–Mo–PGE mineralization in the black shales of the Lower Cambrian Niutitang formation, South China. Ore Geol. Rev. 67, 158–169.
Han, T., Fan, H.F., Zhu, X.Q., Wen, H.J., Zhao, C.H., Xiao, F., 2017. Submarine hydrothermal contribution for the extreme element accumulation during the Early Cambrian, South China. Ore Geol. Rev. 86, 297–308.
Han, T., Fan, H.F., Wen, H.J., 2018. Dwindling vanadium in seawater during the early Cambrian, South China. Chem. Geol. 492, 20–29.
Hoek, J., Reysenbach, A.L., Habicht, K.S., Canfield, D.E., 2006. Effect of hydrogen limitation and temperature on the fractionation of sulfur isotopes by a deep-sea hydrothermal vent sulfate-reducing bacterium. Geochim. Cosmochim. Acta 70, 5831–5841.
Jiang, S.Y., Yang, J.H., Ling, H.F., Chen, Y.Q., Feng, H.Z., Zhao, K.D., Ni, P., 2007a. Extreme enrichment of polymetallic Ni-Mo-PGE-Au in lower Cambrian black shales of South China: an Os isotope and PGE geochemical investigation. Palaeogeogr. Palaeoclimatol. Palaeoecol. 254, 217–228.
Jiang, S.Y., Zhao, K.D., Li, L., Ling, H.F., Zhu, M.Y., 2007b. Highly metalliferous carbonaceous shale and Early Cambrian seawater: COMMENT and REPLY. Geology 35, e158–e159.
Jin, C.S., Li, C., Algeo, T.J., Planavsky, N.J., Cui, H., Yang, X.L., Zhao, Y.L., Zhang, X.L., Xie, S.C., 2016. A highly redox-heterogeneous ocean in South China during the Early Cambrian (~529–514 Ma): implications for biota-environment co-evolution. Earth Planet. Sci. Lett. 441, 38–51.
Johnson, C.A., Emsbo, P., Poole, F.G., Rye, R.O., 2009. Sulfur- and oxygen-isotopes in sediment-hosted stratiform barite deposits. Geochim. Cosmochim. Acta 73, 133–147.
Johnson, C.A., Slack, J.F., Dumoulin, J.A., Kelley, K.D., Falck, H., 2018. Sulfur isotopes of host strata for Howards Pass (Yukon–Northwest Territories) Zn-Pb deposits implicate anaerobic oxidation of methane, not basin stagnation. Geology 46, 619–622.
Jørgensen, B.B., Beulig, F., Egger, M., Petro, C., Scholze, C., Røy, H., 2019. Organoclastic sulfate reduction in the sulfate-methane transition of marine sediments. Geochim. Cosmochim. Acta 254, 231–245.
Kampschulte, A., Strauss, H., 2004. The sulfur isotopic evolution of Phanerozoic seawater based on the analysis of structurally substituted sulfate in carbonates. Chem. Geol. 204 (3–4), 255–286.
Kump, L.R., Pavlov, A., Arthur, M.A., 2005. Massive release of hydrogen sulfide to the surface ocean and atmosphere during intervals of oceanic anoxia. Geology 33, 397–400.
Large, R.R., Bull, S.W., McGoldrick, P.J., Walters, S., 2005. Stratiform and Strata-Bound Zn-Pb-Ag deposits in Proterozoic Sedimentary Basins, Northern Australia. Econ. Geol. 100, 931–963.
Leach, D.L., Sangster, D.F., Kelley, K.D., Large, R.R., Garven, G., Allen, C.R., Gutzmer, J., Walters, S., 2005. Sediment-hosted lead-zinc deposits: a global perspective. Econ. Geol. 100, 561–607.
Leach, D.L., Bradley, D.C., Huston, D., Pisarevsky, S.A., Taylor, R.D., Gardoll, S.J., 2010. Sediment-hosted lead-zinc deposits in earth history. Econ. Geol. 105, 593–625.
Leavitt, W.D., Halevy, I., Bradley, A.S., Johnston, D.T., 2013. Influence of sulfate reduction rates on the Phanerozoic sulfur isotope record. Proc. Natl. Acad. Sci. (USA) 110, 11244–11249.
Lehmann, B., Nagler, T.F., Holland, H.D., Wille, M., Mao, J.W., Pan, J.Y., Ma, D.S., Dulski, P., 2007. Highly metalliferous carbonaceous shale and Early Cambrian seawater. Geology 35, 403–406.
Lehmann, B., Frei, R., Xu, L.G., Mao, J.W., 2016. Early Cambrian black shale-hosted Mo-Ni and V mineralization on the rifted margin of the Yangtze Platform, China:

reconnaissance chromium isotope data and a refined metallogenic model. Econ. Geol. 111, 89–103.
Leng, C.B., Zhang, X.C., Huang, Z.L., Huang, Q.Y., Wang, S.X., Ma, D.Y., Luo, T.Y., Li, W.B., 2018. Geology, Re-Os ages, sulfur and lead isotopes of the Diyanqinamu porphyry Mo deposit, Inner Mongolia, NE China. Econ. Geol. 110, 557–574.
Li, C., Love, G.D., Lyons, T.W., Fike, D.A., Sessions, A.L., Chu, X., 2010. A stratified redox model for the Ediacaran ocean. Science 328, 80–83.
Li, S.R., Gao, Z.M., 2000. Source tracing of noble metal elements in lower Cambrian black rock series of Guizhou-Hunan Provinces, China. Sci. D China Earth Sci. 43, 625–632.
Li, Y.Y., 1997. The Geological characteristics of sea-floor exhalation-sedimentary Chert in Lower Cambrian Black Shales in Dayong-Cili Area, Hunan Province. Acta Petrol. Sin. 13, 121–126.
Li, Z.X., Bogdanova, S.V., Collins, A.S., Davidson, A., Waele, B.D., Ernst, R.E., Fitzsimons, I.C.W., Fuck, R.A., Gladkochub, D.P., Jacobs, J., Karlstrom, K.E., Lu, S., Natapov, L.M., Pease, V., Pisarevsky, S.A., Thrane, K., Vernikovsky, V., 2008. Assembly, configuration, and break-up history of Rodinia: a synthesis. Precambrian Res. 160, 179–210.
Lowenstein, T.K., Hardie, L.A., Timofeeff, M.N., Demicco, R.V., 2003. Secular variation in seawater chemistry and the origin of calcium chloride basinal brines. Geology 31, 857–860.
Lott, D.A., Coveney Jr., R.M., Murowchick, J.B., Grauch, R.I., 1999. Sedimentary exhalative nickel-molybdnum ores in South China. Econ. Geol. 94, 1051–1066.
Lyons, T.W., Gellatly, A.M., McGoldrick, P.J., Kah, L.C., 2006. Proterozoic sedimentary exhalative (SEDEX) deposits and links to evolving global ocean chemistry. Geol. Soc. Am. 198, 169–184.
Lyons, T.W., Reinhard, C.T., Planavsky, N.J., 2014. The rise of oxygen in Earth's early ocean and atmosphere. Nature 506, 306–315.
Magnall, J.M., Gleeson, S.A., Hayward, N., Rocholl, A., 2020. Massive sulfide Zn deposits in the Proterozoic did not require euxinia. Geochem. Persp. Let. 13, 19–24.
Magnall, J.M., Gleeson, S.A., Stern, R.A., Newton, R.J., Poulton, S.W., Paradis, S., 2016. Open system sulphate reduction in a diagenetic environment – Isotopic analysis of barite ($\delta^{34}S$ and $\delta^{18}O$) and pyrite ($\delta^{34}S$) from the Tom and Jason Late Devonian Zn–Pb–Ba deposits, Selwyn Basin, Canada. Geochim. Cosmochim. Acta 180, 146–163.
Marques, A.F.A., Barriga, F.J.A.S., Scott, S.D., 2007. Sulfide mineralization in an ultramafic rock hosted seafloor hydrothermal system: from serpentinization to the formation of Cu–Zn–(Co)-rich massive sulfides. Mar. Geol. 245, 20–39.
McDermott, J.M., Ono, S., Tivey, M.K., Seewald, J.S., Shanks III, W.C., Solow, A.R., 2015. Identification of sulfur sources and isotopic equilibria in submarine hot-springs using multiple sulfur isotopes. Geochim. Cosmochim. Acta 160, 169–187.
Melekestseva, I.Y., Zaykov, V.V., NimisTret'Yakov G.A., Tessalina S.G., P., 2013. Cu–(Ni–Co–Au)-bearing massive sulfide deposits associated with mafic–ultramafic rocks of the Main Urals Fault, South Urals: geological structures, ore textural and mineralogical features, comparison with modern analogs. Ore Geol. Rev. 52, 18–36.
Murowchick, J.B., Coveney Jr, R.M., Grauch, R.I., Eldridge, C.S., Shelton, K.L., 1994. Cyclic variations of sulfur isotopes in Cambrian stratabound Ni-Mo-(PGE-Au) ores of Southern China. Geochim. Cosmochim. Acta 58, 1813–1823.
Pašava, J., Kříbek, B., Vymazalová, A., Sýkorová, I., Žák, K., Orberger, B., 2008. Multiple sources of metals of mineralization in lower Cambrian black shales of south china: evidence from geochemical and petrographic study. Resour. Geol. 58, 25–42.
Peter, J.M., Shanks III, W.C., 1992. Sulfur, carbon, and oxygen isotope variations in submarine hydrothermal deposits of Guaymas basin, Gulf of California, USA. Geochim. Cosmochim. Acta 56, 2025–2040.
Pufahl, P.K., Hiatt, E.E., 2012. Oxygenation of the Earth's atmosphereeocean system: a review of physical and chemical sedimentologic responses. Mar. Petrol. Geol. 32, 1–20.
Qiu, W.J., Zhou, M.F., Li, X.C., Williams-Jones, A.E., Yuan, H., 2018. The genesis of the Giant Dajiangping SEDEX-type pyrite deposit, South China. Econ. Geol. 113, 1419–1446.
Rees, C.E., 1970. The sulphur isotope balance of the ocean: an improved model. Earth Planet. Sci. Lett. 7, 366–370.
Sim, M.S., Bosak, T., Ono, S., 2011. Large sulfur isotope fractionation does not require disproportionation. Science 333, 74–77.
Sim, M.S., Paris, G., Adkins, J.F., Orphan, V.J., Sessions, A.L., 2017. Quantification and isotopic analysis of intracellular sulfur metabolites in the dissimilatory sulfate reduction pathway. Geochim. Cosmochim. Acta 206, 57–72.
Slack, J.F., Dumoulin, J.A., Schmidt, J.M., Young, L.E., Rombach, C.S., 2004. Paleozoic sedimentary rocks in the Red Dog Zn-Pb-Ag district and vicinity, Western Brooks Range, Alaska: provenance, deposition, and metallogenic significance. Econ. Geol. 99, 1385–1414.
Sperling, E.A., Frieder, C.A., Raman, A.V., Girguis, P.R., Levin, L.A., Knoll, A.H., 2013. Oxygen, ecology, and the Cambrian radiation of animals. Proc. Natl. Acad. Sci. (USA) 110, 13446–13451.
Thode, H.G., Kleerekoper, H., McElcheran, D., 1951. Isotope fractionation in the bacterial reduction of sulphate. Research 4, 581–582.
Wang, J.G., Chen, D.Z., Yan, D.T., Wei, H.Y., Xiang, L., 2012. Evolution from an anoxic to oxic deep ocean during the Ediacaran-Cambrian transition and implications for bioradiation. Chem. Geol. 306–307, 129–138.
Wen, H.J., Fan, H.F., Zhang, Y.X., Cloquet, C., Carignan, J., 2015. Reconstruction of Early Cambrian ocean chemistry from Mo isotopes. Geochim. Cosmochim. Acta 164, 1–16.
Westall, F., Hickman-Lewis, K., Hinman, N., Gautret, P., Campbell, K.A., Bréhéret, J.G., Foucher, F., Hubert, A., Sorieul, S., Dass, A.V., Kee, T.P., Georgelin, T., Brack, A., 2018. A hydrothermal-sedimentary context for the origin of life. Astrobiology 18, 1–35.
Wignall, P.B., Newton, R., 1998. Pyrite framboid diameter as a measure of oxygen deficiency in ancient mudrocks. Am. J. Sci. 298, 537–552.
Wilkin, R.T., Barnes, H.L., Brantley, S.L., 1996. The size distribution of framboidal pyrite in modern sediments: an indicator of redox conditions. Geochim. Cosmochim. Acta 60, 3897–3912.
Wille, M., Nägler, T.F., Lehmann, B., Schröder, S., Kramers, J.D., 2008. Hydrogen sulphide release to surface waters at the Precambrian/Cambrian boundary. Nature 453, 767–769.
Xu, L.G., Lehmann, B., Mao, J., Qu, W., Du, A., 2011. Re-Os age of polymetallic Ni-Mo-PGE-Au mineralization in early Cambrian black shales of South China-a reassessment. Econ. Geol. 106, 511–522.
Xu, L.G., Lehmann, B., Mao, J.W., 2013. Seawater contribution to polymetallic Ni–Mo–PGE–Au mineralization in Early Cambrian black shales of South China: evidence from Mo isotope, PGE, trace element, and REE geochemistry. Ore Geol. Rev. 52, 66–84.
Xu, D.T., Wang, X.Q., Shi, X.Y., Tang, D.J., Zhao, X.K., Feng, L.J., Song, H.Y., 2020. Nitrogen cycle perturbation coupled with metazoan diversification during the early Cambrian. Palaeoclimatol. Palaeoecol Palaeogeogr. https://doi.org/10.1016/j.palaeo.2019.109392.
Zeng, Z.G., Ma, Y., Chen, S., Selby, D., Wang, X.Y., Yin, X.B., 2017. Sulfur and lead isotopic compositions of massive sulfides from deep-sea hydrothermal systems: implications for ore genesis and fluid circulation. Ore Geol. Rev. 87, 155–171.
Zhao, J., Li, G.B., Selden, P.A., 2019. A poorly preserved fish-like animal from the Chengjiang Lagerstätte (Cambrian Series 2, Stage 3). Palaeogeogr. Palaeoclimatol. Palaeoecol. 520, 163–172.
Zhao, X.K., Wang, X.Q., Shi, X.Y., Tang, D.J., Shi, Q., 2018. Stepwise oxygenation of early Cambrian ocean controls early metazoan diversification. Palaeogeogr. Palaeoclimatol. Palaeoecol. 504, 86–103.
Zhu, M.Y., Yang, A.H., Yuan, X.L., Li, G.X., Zhang, J.M., Zhao, F.C., Anh, S.Y., Miao, L.Y., 2019. Cambrian integrative stratigraphy and timescale of China. Sci. China Earth Sci. 62, 25–60. https://doi.org/10.1007/s11430-017-9291-0.